EMU Notes in Mineralogy, Vol. 16 (2017), Chapter 4, 97–130

Spatially resolved materials characterization with TEM

RICHARD WIRTH

Helmholtz Centre Potsdam, GFZ German Research Centre For Geosciences,
4.3, Telegrafenberg, 14473 Potsdam, Germany, e-mail: wirth@gfz-potsdam.de

Transmission electron microscopy (TEM) is an ideal tool for characterizing materials in terms of chemical composition, micro- and nanostructure as well as crystal structure up to atomic level. The major advantage of TEM is superior spatial resolution. It is possible to obtain chemical composition and structure information from even nm-sized crystals and that allows unambiguous identification of the phases present in a TEM sample. Chemical information is supplied by EDX analysis, electron energy-loss spectroscopy (EELS) and to a small extent by Z-contrast imaging (high-angle annular dark-field imaging – HAADF). Micro- and nanostructure information is provided applying bright-field and dark-field imaging based on diffraction contrast and high-resolution imaging (HREM). Structure information is obtained from selected area electron diffraction (SAED), convergent beam electron diffraction on nm-sized crystals, precession electron diffraction which allows crystal-structure determination and fast Fourier transforms (calculated diffraction-pattern FFT) from high-resolution images.

1. Introduction

This chapter on spatially resolved materials characterization with transmission electron microscopy (TEM) is not to be considered as another contribution to the already existing excellent textbooks on electron microscopy (Hirsch *et al*., 1977; Putnis, 1992; Williams and Carter, 1996; Joy *et al*., 1986; Fultz and Howe, 2001). Rather, it is more focused on applications of TEM methods in the geosciences. Detailed theoretical contributions to the different chapters can be found in the textbooks referenced in the text.

TEM is an ideal tool for identifying unambiguously micrometre- or nanometre-sized crystalline or non-crystalline objects based on their crystal structure and their chemical composition. Phase identification is important but can be demanding, especially the investigation of nanometre-sized inclusions in minerals. For example, nano-inclusions discovered in diamond established novel ideas on the formation of diamonds. The chemical composition of the nano-inclusions found in diamond allowed reconstruction of the fluid or melt composition from which diamond has nucleated and grown (Klein BenDavid *et al*., 2006; Logvinova *et al*., 2008; Kaminsky *et al*., 2009, 2015). It needs to be emphasized, however, that this kind of investigation was feasible only when the focused ion beam (FIB) sample preparation technique was made available for TEM sample preparation. FIB is a site-specific sample preparation technique that allows for sputtering electron transparent foils out of almost any material (Wirth, 2004, 2009).

DOI: 10.1180/EMU-notes.16.4

The basic principle of TEM is that accelerated electrons with a typical kinetic energy of 200 keV penetrate through an electron transparent slice of matter. With geomaterials, FIB-prepared foils of minerals or rock slices are usually 150 nm thick. However, they can also be fabricated thicker as in the case of diamond (up to 250 nm) or substantially thinner (as small as 30 nm) if required. The electron beam penetrating through the sample interacts with the atoms constituting the specimen resulting in diverse scattering events. Recording the different interactions of the primary electrons with electrons or nuclei of the specimen applying suitable detectors allows extraction of structural and chemical information from the sample (Fig. 1). Principally, there are elastically scattered electrons (no momentum transfer from the primary electron onto the target electron) and inelastically scattered electrons (momentum transfer from the primary electron to the target electron or nucleus. Bragg scattered electrons are elastically scattered primary electrons scattered at the outer shell electrons of target atoms thus providing information about the crystal structure and symmetry of the target. Electrons that are elastically scattered at inner shell electrons can be used for Z-contrast imaging using high-angle annular dark field detectors (HAADF). The scattering angle and scattering intensity depend on the atomic number of the scattering atom. Inelastic scattering occurs when a primary electron transfers enough momentum onto an inner shell target electron to excite it into unoccupied states or into the vacuum. Instantaneously, the empty site will be filled with an outer shell electron and the energy difference is emitted as an X-ray photon. Chemical information about the sample can be derived from the excited X-ray photons that are collected with an energy dispersive X-ray detector (EDX). However, excited X-ray photons contain enough energy to excite outer-shell electrons of the same atom, which can then be recorded as Auger electrons (Auger electron spectroscopy). Auger electrons probe the surface chemistry of a specimen. Because of their comparatively low energy they will be absorbed very rapidly if they are excited at a greater depth of the sample. The energy-loss of primary electrons

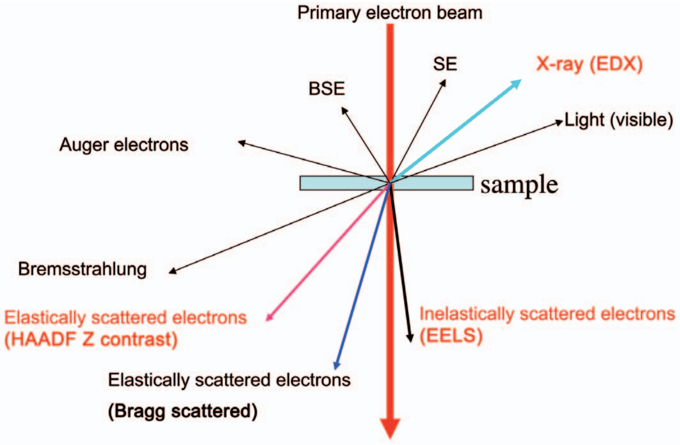

Fig. 1. The interaction of high-energy electrons with matter causes several scattering events that can be used in TEM.

during inelastic scattering can be measured with electron energy-loss spectroscopy (EELS). Inelastic scattering is predominantly forward scattering under low scattering angles (<1°). Secondary electrons (SE), and back-scattered electrons (BSE) usually are not used in TEM applications. Details of the interactions of accelerated electrons with matter are given elsewhere (Williams and Carter, 1996; Fultz and Howe, 2001).

Full characterization of nano-inclusions in minerals requires knowledge of chemical composition and structural properties. Chemical information from the specimen can be derived from EDX analysis, EELS and Z-contrast imaging (HAADF). Diffraction contrast imaging (grain boundaries, dislocations, stacking faults, antiphase domain boundaries), electron diffraction and high-resolution imaging (HRTEM) provide structural information.

2. Chemical composition of materials

2.1. EDX analysis

X-ray photons are generated when an incident primary electron (*e.g.* 200 keV) transfers enough energy to a core electron to eject it from its energy level into an unoccupied state or into the vacuum. If the electron is ejected into the vacuum the atom is ionized. For example, an electron from the innermost copper K-shell requires the energy of 8.98 keV to be ionized (Williams and Carter, 1996). An outer shell electron of higher energy level falls into this empty state thus emitting the energy difference as an X-ray photon. In the case of a Cu$K\alpha_1$ X-ray photon, which is emitted during the transition of an electron from the L_3 level to the K-shell of a copper atom, the energy released is 8.04778 keV (Fultz and Howe, 2001). The X-ray photon that is emitted can be detected using a Li-doped silicon detector. The X-ray photon creates an electron−hole pair in the Si detector. A high voltage applied to the detector causes the electrons moving towards the positive end and the hole that can be considered as positive charge towards the negatively charged side of the silicon crystal thus creating an electrical pulse that can be registered by the detector. More details on Si-Li detectors and their working principles are presented elsewhere (Joy *et al.*, 1986; Williams and Carter, 1996).

The X-ray intensities of the different K or L or M lines of the elements constituting a sample can be measured qualitatively or quantitatively using standard material. The X-ray intensity of a particular element concentration depends on the X-ray fluorescence yield of the element. The X-ray fluorescence yield, ω, is a measure for the number of electrons needed to excite one single X-ray photon (Fig. 2). For example, for carbon (Z = 6) $\omega = 10^{-3}$, *i.e.* 1000 electrons are needed to excite 1 X-ray photon. An element with a higher atomic number such as Germanium (Ge) requires only 2 electrons to excite 1 X-ray photon (ω = 0.5). For elements with an atomic number <30, Auger electrons will predominate over X-ray photons thus resulting in a low X-ray fluorescence yield of the element.

2.1.1. Quantitative analysis in analytical electron microscopy (AEM)

Quantitative analysis in TEM is based on the Cliff-Lorimer equations (Cliff and Lorimer, 1975):

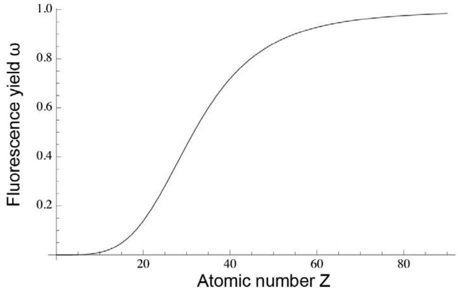

Fig. 2. X-ray fluorescence yield depending on the atomic number Z of an element.

$$\frac{C_A}{C_B} = k_{AB}\frac{I_A}{I_B} \tag{1}$$

$$C_A + C_B = 1 \tag{2}$$

The Cliff-Lorimer equations relate the ratio of the concentration of two elements *A* and *B* in the sample to the measured X-ray intensities, *I*, of the elements *A* and *B* in the sample. The factor k_{AB} needs to be determined from a standard reference material. It considers the ionization cross-section σ, the fraction of the total line intensity measured, the absorption of the X-ray photons depending on sample thickness and some detector properties. Quantitative X-ray analysis with TEM is described in great detail in the textbook by Joy, Romig and Goldstein (1986). Standard reference materials for calibration of the k_{AB}-factor can be a mineral grain that was analysed by the electron probe microanalysis (EPMA), or a part of the sample was analysed by some other chemical method (*e.g.* wet chemistry, inductively coupled plasma mass spectrometry [ICPMS], *etc.*) to determine its chemical composition. After that, a TEM foil can be cut with FIB technique from the same area that was measured with the microprobe. That TEM foil is then used as a standard reference material. Because of the strong influence of matrix effects on the detected X-ray intensity, it is crucial to use standard materials with chemical composition and structure at least close to that of the unknown sample. The number of the k_{AB}-factor is valid only if the sample foil has approximately the same thickness as the standard foil, because the value of the k_{AB}-factor increases with increasing foil thickness (Fig. 3). In geomaterials k_{AB} factors are usually based on Si (B), and in materials sciences very often Fe is used as reference (B).

Focused ion beam-prepared TEM foils are ideal for line scans and element mapping because of their homogeneous thickness. The measured intensities of individual X-ray lines in element maps or line scans are interpretable only if the sample thickness does not change and the X-ray intensity is related only to the concentration of the element in the sample and not to varying sample thickness.

2.1.2. Detection limit of elements analysed and total error calculation of the results

The detection limit of an element in energy dispersive X-ray analysis (EDX) is an important factor when measuring low element concentrations. In general, the detection

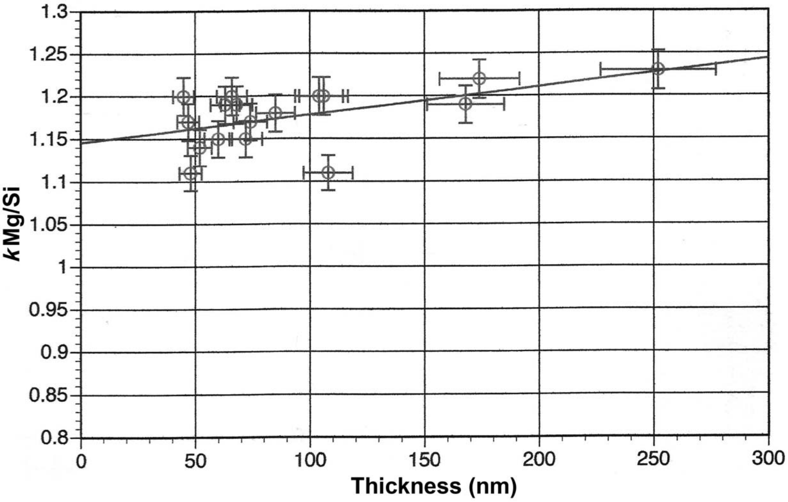

Fig. 3. Dependence of the k_{AB} factor – here $k_{\mathrm{Mg/Si}}$ – on the thickness of the TEM foil.

limit is much higher (100s of ppm) than that of electron microprobe analysis (10s of ppm) using wavelength dispersive spectroscopy (WDS). Before the concentration detection limit can be determined it is mandatory to decide if the observed peak intensity is statistically valid peak intensity. A peak is statistically valid if the following criterion is fulfilled:

$$I_A - I_b^A \geq 3\sqrt{2I_b^A} \tag{3}$$

where I_A is the measured intensity of the element A in the EDX spectrum and I_b^A is the background intensity of that peak. The concentration detection limit C_{DL} of an element with the known concentration C_A in a sample is given by the equation:

$$C_{\mathrm{DL}} = C_A \frac{3\sqrt{2I_b^A}}{I_A - I_b^A} \quad \text{(Goldstein and Williams, 1989)} \tag{4}$$

For example, the detection limit of Pt-group elements in sulfide matrix using EDX is ~700 ppm (Wirth *et al.*, 2013).

2.1.3. Total error in X-ray analysis analytical electron microscopy (AEM)

Another very important criterion to evaluate data from EDX analyses is to evaluate the statistical error and the absolute error of the measurement. Quantitative EDX analysis requires calculation of the statistical and the absolute errors for both the k_{AB} factor and the concentration of the elements in the sample and addition of both errors. Low X-ray intensities resulting in poor counting statistics are a major source of significant statistical error. Gaussian behaviour describes the counting statistics. That is $\sigma = \sqrt{N}$

with N the number of accumulated counts. At the 3σ confidence level (99.73%) the error in the number of accumulated counts is $3\sigma = \sqrt{N}$. Then, the relative error in the number of counts is $3\sqrt{N}/N \times 100$. A relative error in the intensity of a particular element of ± 3% is achieved by 10,000 accumulated counts above background. The error in the measured concentration of an element in a mineral is larger in a single measurement than in n individual measurements. The same holds true for the determination of the k_{AB} factor. Therefore, n measurements should be done to minimize the error. The relative error of k_{AB} based on a 99.73% confidence level is determined as follows:

$$\%\ \text{error} = \left[\frac{t_{99}^{n-1}}{\sqrt{n}}\frac{s}{\bar{k}_{AB}}\right] \times 100 \tag{5}$$

In that equation $t_{99}{}^{n-1}$ is the Student t value calculated from n analyses at the 99.73 % confidence level (3σ) (*cf.* Brownlee, 1960), s is the standard deviation from n measurements, and k_{AB} is the mean of k_{AB} from n spectra. That calculation accounts for the relative error of the k_{AB} factor. Error calculation of the concentration of an element in a mineral with n measurements follows the same equation.

$$\%\ \text{error} = \left[\frac{t_{99}^{n-1}}{\sqrt{n}}\frac{s}{\bar{C}_A}\right] \times 100 \tag{6}$$

Here again s is the standard deviation of n individual measurements and C_A is the mean of the concentration of the element A from each of the n spectra.

Errors add up, that means the relative error of k_{AB} and the relative error of C_A must be added up to a total error. Table 1 shows an example of the error calculation of MgO, Al_2O_3, CaO and TiO_2 measured from orthopyroxene using an orthopyroxene standard. Details and examples of error calculation are presented elsewhere (Brownlee, 1960; Goldstein and Williams, 1989; Williams and Carter, 1996).

2.2. High-angle annular dark-field imaging (HAADF)

The interaction of primary electrons with matter results in scattering of the primary electrons at the inner and outer shell (K) electrons of an atom. The scattering angle of the inner shell electrons is larger (>>10 mrad) than those scattered at the outer shell electrons (<10 mrad). A high-angle annular dark field detector (HAADF), a semiconductor device, collects the scattered electrons. The intensity of the primary electrons scattered at the inner shell electrons of an atom and detected by HAADF depends on the atomic number (Z). A detector that collects electrons scattered at the inner shell electrons of an atom produces a Z-contrast image. A typical HAADF detector is a semiconductor device designed as a disk with a hole in the centre. Because of the much smaller scattering angle of the electrons that were scattered at the outer shell electrons of an atom (Bragg scattered electrons causing diffraction contrast) the Bragg scattered electrons might fall through the hole and will not contribute to the image contrast. It depends on the selected camera length of the TEM and which kind of electrons is collected using the HAADF detector. Using a short camera length (*e.g.*

Table 1. Error calculation of an EDX analysis from OPX.

Error of the k_{AB} factor from n measurements

n = 17	$k_{\mathrm{Mg/Si}}$	$k_{\mathrm{Al/Si}}$	$k_{\mathrm{Ca/Si}}$	$k_{\mathrm{Ti/Si}}$
$\bar{x}$	1.18	1.05	0.88	0.78
s	0.035	0.103	0.173	0.692
Error (%)	1.85	6.11	12.2	55.2

n = 17	MgO	Al_2O_3	CaO	TiO_2
$\bar{x}$	33.16	4.38	0.89	0.12
s	0.56	0.40	0.20	0.09
Error (%)	1.05	5.7	14.5	48.4
Total rel. error (%)	2.9	11.81	26.7	103.6

$\bar{x}$ = mean of n measurements
s = standard deviation

75 mm) the detector collects the high-angle scattered electrons only, thus providing a Z-contrast image (Fig. 4). A camera length in the range of 220–330 mm collects both high-angle scattered electrons (Z contrast) and Bragg scattered electrons thus displaying Z-contrast plus diffraction contrast (dislocations, grain boundaries) (Fig. 4).

The resolution of the HAADF imaging depends on the sample thickness and should not exceed 40 nm for high-resolution imaging. Recorded scattering intensity depends also on sample thickness. Pores in a sample are visible in the image as slightly darker contrast because at the location of the pore the sample thickness is reduced and thus fewer electrons are scattered. Note that in TEM bright-field (BF) imaging the contrast is reversed and pores will appear brighter than the matrix. In that case, the reduced thickness will cause less absorption of electrons resulting in a brighter image contrast. HAADF imaging is very sensitive for nano-inclusions of high atomic number elements in a silicate or sulfide matrix. For example, Pb spheres of only a few nanometres in diameter as inclusions in a zircon matrix can be identified easily in a HAADF image even at lower magnification due to the high brightness (Z-contrast) in the HAADF image (Fig. 5) (Kusiak *et al.*, 2015).

2.3. Electron energy-loss spectroscopy (EELS)

Primary electrons with a typical energy of 200 keV pass through the sample interacting with the electrons of the atoms that constitute the sample. Along with these interactions inelastic scattering events occur. During inelastic scattering the primary electron loses energy because it transfers momentum onto a target atom or electron. The energy loss of the primary electrons is measured with electron energy-loss spectroscopy (EELS).

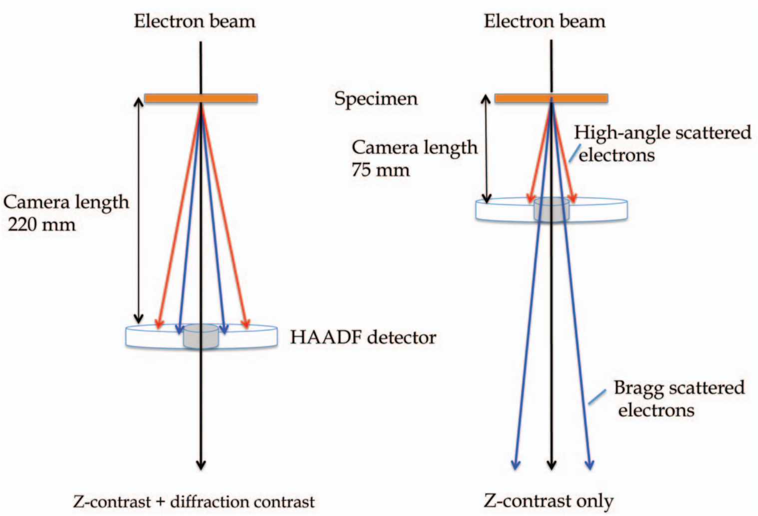

Fig. 4. The position of the HAADF detector defined by the camera length determines which kind of scattered electrons are detected. At a small camera length (*e.g.* 75 mm) only those electrons that were scattered at the inner shell electrons of the sample are collected displaying a Z-contrast image. At a larger camera length (*e.g.* 220 mm) additionally, the Bragg scattered electrons are collected thus producing a Z-contrast plus diffraction contrast image.

A typical EEL spectrum as shown in Fig. 6 can be subdivided in three different energy regions:

1. The *zero-loss peak* representing elastically forward scattered electrons or non-scattered electrons without energy-loss.
2. The *low-loss region* with the plasmon peak extending up to an energy region of ~50 eV representing electrons that have interacted with the weakly bonded outer-shell electrons or the delocalized electrons in a sample.
3. The energy region above 50 eV, the so-called *core-loss region*, represents those primary electrons that have interacted with the more tightly bonded electrons of the inner shells (K, L, M) of an atom.

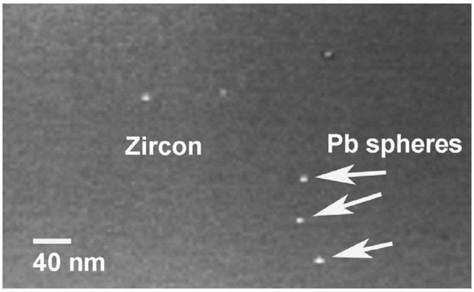

Fig. 5. HAADF Z-contrast image displaying Pb-nanospheres in zircon.

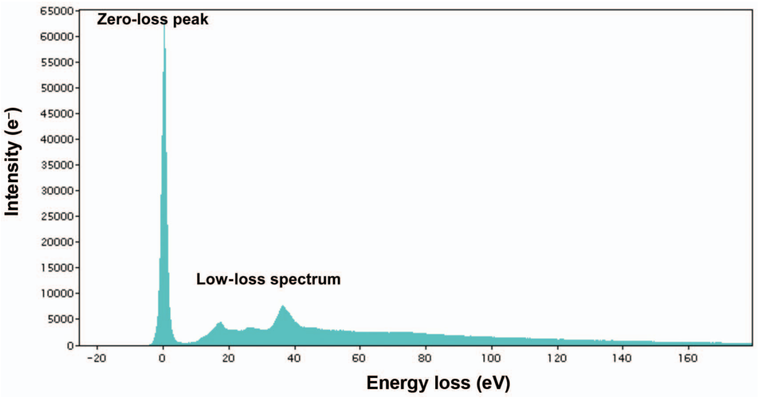

Fig. 6. Electron energy-loss (EEL) spectrum. Zero-loss peak that represents the unscattered and elastically scattered electrons plus low-loss spectrum.

The different energy-loss regions provide special and characteristic information about the atoms constituting the specimen. The zero-loss peak can be used to determine the energy resolution of the spectrometer. For example, electrons emitted from a field emission gun (FEG) electron source usually have an energy resolution of ~0.9 eV (full width at half maximum of the peak (FWHM)).

The plasmon peak characterizes the low-loss spectrum. In that case the primary electrons transfer energy to the weakly bonded outer shell electrons or the free electron gas in metals thus causing longitudinal collective oscillations of these electrons. The typical energy loss of these electrons is in the range 5–40 eV (Fig. 6).

An electron can be ejected into the vacuum, thus ionizing the atom, when primary electrons transfer sufficient energy to an electron of the K, L, M or an outer shell. The energy loss due to ionization or just to excite an inner shell electron to an unoccupied state in an outer shell level defines the high-loss spectrum or core-loss spectrum (Fig. 7). In Fig. 7 the core loss spectrum of NiO is displayed in the energy range of the Ni-$L_{3,2}$ edge. The edge onset of the Ni-L_3 edge is at 855 eV. One of the 2s or the 2p electrons of the L-shell of Ni has been excited and it could fill an unoccupied 3d state (Ni has two unoccupied 3d states). To excite a 1s electron from the oxygen K-shell 532 eV must have been transferred from the primary electron to the excited electron. In the case of oxygen 532 eV is the critical ionization energy, E_c, to overcome the ionization threshold. The 1s electron at the K-shell can be ejected into the vacuum or into an unoccupied 2p state (oxygen has 2 unoccupied p states on the L shell). The scattering angle

$$\Theta_E = \frac{E}{2E_0} \tag{7}$$

of the scattered primary electron is in general very small, and in the case of oxygen it is 1.3 mrad. E is the energy-loss of the primary electron at the onset of the edge (*e.g.* O-K edge 532 eV) after momentum transfer, and E_0 is the electron energy of the incident

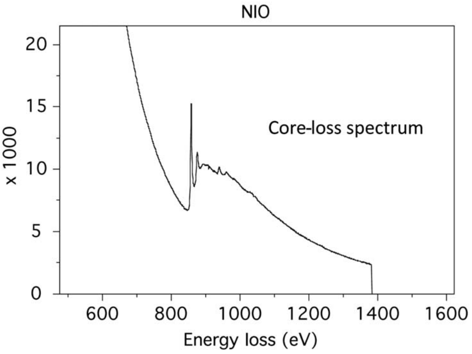

Fig. 7. EEL spectrum. Core-loss spectrum showing the Ni-L3,2 edge.

electron beam (200,000 eV). The critical ionization energy, E_c, defined by the edge onset has the greatest probability of ionizing an atom. That means, with increasing transferred energy the probability of ionizing an atom or exciting a 1s electron into an unoccupied state decreases. The scattering cross section σ for such a scattering event decreases with increasing energy-loss thus reducing the probability of ionization. In the case of a hydrogen atom the energy-loss spectrum would resemble a saw tooth curve with a sharp onset and a gradual decrease with increasing energy-loss (Fig. 8a). However, in a sample with finite thickness the primary electron will experience multiple scattering resulting in a plural scattering background (Fig. 8b). The core-loss edge is superimposed onto the background. Consequently, good quality EEL spectra require thin samples (<<100nm) for good peak/background ratios. Usually, the total edge shape, which is termed the energy-loss near edge structure (ELNES), extends ~50 eV from the edge onset to higher energy losses. The ELNES of a particular atom in a crystal or any solid-state material is more complicated and contains information about the electronic structure of the atom. Iron is a good example to demonstrate that. The edge onset can vary when changing the valence state of an ion, which is then called 'chemical shift'. For example, a valence change of iron from Fe^{2+} to Fe^{3+} will alter the

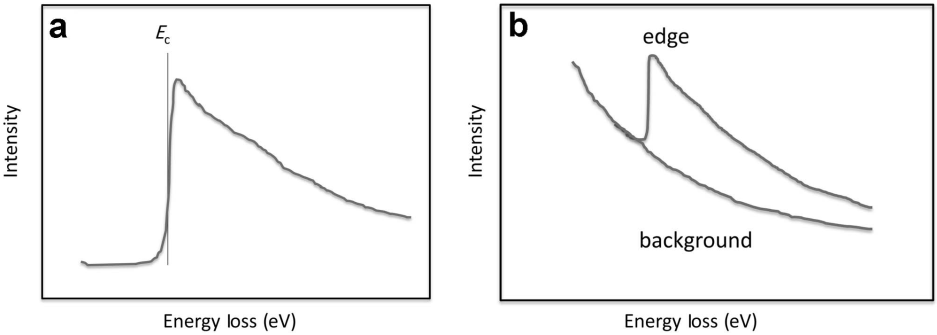

Fig. 8. EEL spectrum. (a) Idealized hydrogen K-edge spectrum with the critical energy E_c to remove the 1s electron from its K-shell position. (b) Idealized core-loss edge superimposed on the background.

screening of the positive charge of the nucleus by the electrons. If there is one electron less present (Fe^{3+}) screening the charge of the nucleus, the inner shell electrons from the K, L and M shells will be bonded slightly more strongly to the nucleus, thus higher energy is required to excite an electron from the L shell to an empty state on the 3d level of the M shell. In the EEL spectrum of Fe^{3+} the onset of the $L_{3,2}$ edge is shifted ~1.7 eV to higher energies (707.8 eV Fe^{2+} and 709.5 eV Fe^{3+}; van Aken *et al.*, 1998). The valence state of an ion can be determined from an EEL spectrum.

ELNES can also be used as a fingerprint to identify individual phases. This has been proposed and demonstrated previously (Taftø and Zhu, 1982; Rask *et al.*, 1987; Kurata *et al.*, 1993; Garvie *et al.*, 1994). ELNES of the carbon C-K edge is a very good example of how the edge structure can be used as a fingerprint to identify a polymorph. The C-K edges of amorphous carbon, graphite and diamond are significantly different in edge-onset and near edge structure and can be used to discriminate between the carbon phases without using electron diffraction. The basic component of graphite and amorphous carbon are planar rings with 6 carbon atoms. Graphite and amorphous carbon are characterized by strong σ-bonds or sp^2 hybrid orbitals within the hexagonal ring structure. Additionally, there are non-hybridized p_z orbitals forming the π-bonds normal to the hexagonal sheets. The EEL spectrum of graphite and amorphous carbon contains and displays the information about the two different bond types σ- and π-bonds. In the EEL spectrum, there is a pre-peak with an edge-onset at 284 eV, which represents the π-bonds, followed by a stronger peak with an onset at ~290 eV representing the sp^2-bonds or σ-bonding (Fig. 9a). The only difference between the EEL spectra of graphite and amorphous carbon is that the sp^2-related peak is more structured showing 3 peaks, whereas the sp^2-related peak in amorphous carbon is smooth and rounded (Fig. 9b). The π-bond related peak at 284 eV appears in both the spectra of graphite and amorphous carbon. Pure sp3 hybrid bonds without π-bonding characterize diamond. Therefore, in diamond, the pre-peak due to π-bonds is absent and the edge-onset of the C-K edge representing the sp^3 bonds is at ~289 eV followed by a second peak with its maximum at 299.8 eV and a third peak with a maximum at ~305 eV (Fig. 9c). The carbon C-K edge allows identification of amorphous carbon, graphite or diamond using the ELNES of the carbon C-K edge as a fingerprint.

The individual core-loss edges can be used for high-resolution element mapping. There are two methods of element mapping: a three-windows technique and a two-windows jump ratio technique. The basic procedure of the three-windows technique is as follows (using the O-K edge as an example). An image is acquired applying an energy window of 30 eV to the O-K edge with an offset of 15 eV towards higher energy loss from the edge onset (532 eV). Additionally, two windows each 30 eV wide are placed at lower energy loss than the edge onset with an offset of 18 eV and 48 eV, respectively, in regard to the onset of the O-K edge. The two pre-edge windows are used to calculate the background intensity and to subtract the background intensity from the intensity at the O-K edge (*Digital Micrograph* software package®). The residual O-K edge intensity represents the oxygen concentration in the image.

The two-windows technique is different. In that case, only two images are acquired with a defined width of the energy windows and offset from the edge onset. The post-

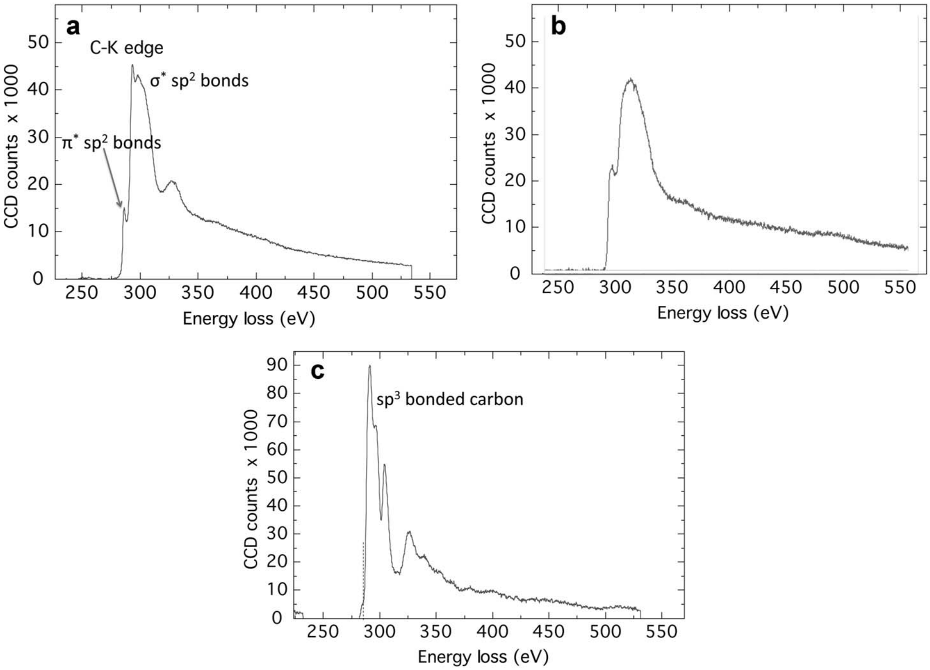

Fig. 9. EEL spectrum of carbon C-K edge. (a) Carbon C-K edge of graphite. Note the pre-edge peak (arrow) that indicates the π bonds in graphite. (b) Carbon C-K edge of amorphous carbon. Both bond types π and σ bonds are visible; the pronounced edge structure of the σ bonds is converted into a rounded peak, however. (c) Carbon C-K edge structure of diamond. The signal from the π electrons is almost absent and the σ bonds are replaced by sp^3 bonding. The signature of the carbon C-K edge can be used as a fingerprint of the carbon phase present.

edge image is divided by the pre-edge image creating a jump ratio image, which is very sensitive to thickness variations. An example of element mapping with EELS using the three windows technique is shown in Fig. 10a,b. A narrow platelet in diamond, ~300 nm wide, is composed of graphite and Fe-carbide (Fe_3C). Element maps of the C-K edge (Fig. 10b) and the Fe-$L_{3,2}$ edge (Fig. 10a) show the distribution of graphite and Fe-carbide within that narrow platelet on a nanometre scale (Kaminsky and Wirth, 2011).

Another useful application of EELS is the measurement of the local sample thickness of a TEM foil. The knowledge of the foil thickness is required for quantitative EDX analysis incorporating absorption correction. The amount of inelastic scattering in a sample increases with increasing specimen thickness. That means that the ratio between the intensity of the primary unscattered electrons and/or elastically scattered electrons and the intensity of the inelastically scattered electrons contains information about the sample thickness. The sample thickness, *t*

$$t/\lambda = \ln(I_{\text{tot}}/I_0) \tag{8}$$

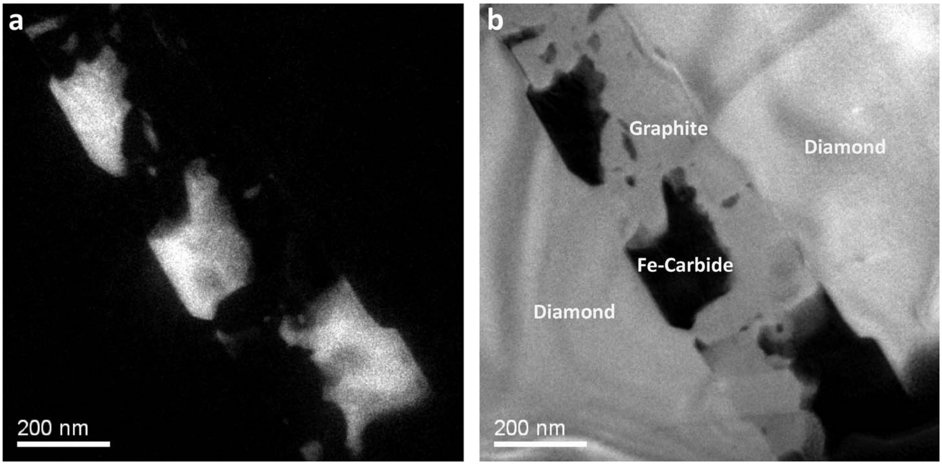

Fig. 10. EELS element mapping applying the three-window technique. Fe carbide precipitated in diamond. (a) Element map of Fe using the Fe-$L_{3,2}$ edge. (b) Element map of carbon using the C-K edge.

is the ln of the ratio of the total intensity of the spectrum, I_{tot}, and the intensity of the zero loss peak, I_0, multiplied by the mean free path, λ, of the electrons in the sample. Details of the calculation of λ are presented elsewhere (Egerton, 1996; Williams and Carter, 1996). There are several other applications of EELS, which are beyond the scope of this chapter and can be found elsewhere together with many fundamental details of EEL spectroscopy and technical descriptions (Joy *et al*., 1986; Egerton, 1996; Williams and Carter, 1996).

3. Structural information

3.1. Electron diffraction

Primary electrons penetrating through a specimen are scattered elastically at the outer shell electrons of the atoms constituting the sample. This kind of electron scattering is called Bragg scattering, and if the conditions of the Bragg equation

$$n\lambda = 2d\sin\theta \tag{9}$$

are fulfilled, diffraction intensity can be recorded (film, image plate, CCD camera). In the Bragg equation n is the order of a reflection (*e.g.* (100), (200)....), λ is the wavelength of the electrons at a given accelerating voltage (*e.g.* 0.00251 nm relativistic wavelength at 200 keV), d is the spacing of the reflecting lattice plane (hkl), and θ is the scattering angle. In conventional electron diffraction patterns the specimen is illuminated with a parallel electron beam using the condenser lenses to adjust illumination. The objective lens focuses the diffracted electrons in the back focal plane forming the first diffraction pattern, which is finally magnified and imaged onto the fluorescence screen by the subsequent lens systems. There are two techniques to generate electron diffraction patterns. The most commonly used technique is the selected area electron diffraction pattern (SAED) with parallel illumination of the sample. SAED contains structural information from a scattering volume that is defined by a diffraction aperture (10 up to 800 μm in diameter). The SAED pattern consists of discrete and symmetrically arranged scattering intensity spots (Fig. 11a). The convergent beam electron diffraction (CBED) technique uses a focused electron beam thus allowing electron diffraction from even nanometre-sized crystals. The scattering volume is defined by the size of the electron beam and not by an aperture. The electron diffraction pattern is composed of diffraction discs in the back focal plane (Fig. 11b). The diameter of the discs depends on the electron beam size and the camera length used. The CBED patterns are evaluated using the same procedure as for the SAED pattern. Measuring the distances between the diffraction spots or between the discs provides the length of a diffraction vector $\vec{g}$ in reciprocal space. The d spacing d_{hkl} (real space) is calculated by applying the equation

$$\lambda L = \vec{g} d_{hkl} \tag{10}$$

with L the camera length (mm), λ the relativistic wavelength of the accelerated electron (200 kV; 0.00251 nm), $\vec{g}$ (mm) and d_{hkl} (nm). Usually, electron diffraction patterns do not represent the true scattering intensity because of dynamical scattering conditions (thick sample); therefore, crystal symmetry and crystal structure determination is almost impossible. That problem has been overcome by introducing precession electron diffraction (Vincent and Midgley, 1994). The precession technique is equivalent to the Buerger precession technique applied in X-ray crystallography where the specimen is precessed with respect to the incident X-ray beam (Buerger, 1970). In a TEM, the sample is static and the electron beam is precessing around the optical axis on a conical surface. As a result of that precession more reflections in the reciprocal space appear, the scattered intensity is closer to the real scattering intensity and the final diffraction pattern is much closer to true kinematic diffraction

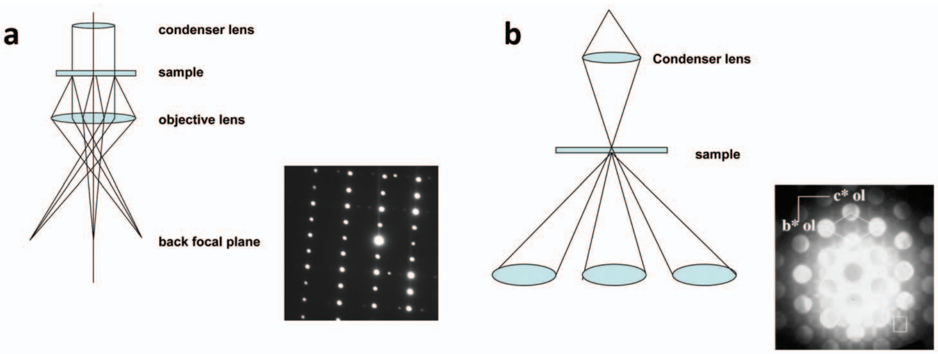

Fig. 11. Electron diffraction. (a) Microscope setting for selected area electron diffraction (SAED). Note the diffracted electrons form sharp reflection spots on the viewing screen. (b) Microscope setting for convergent beam electron diffraction (CBED). Note the diffraction discs.

conditions. With precession electron diffraction the occurrence of forbidden reflections due to multiple scattering is reduced significantly thus allowing determination of the space group. With the precession electron diffraction technique it is possible to perform structure analysis even from nanometre-sized crystals (Koch-Müller *et al.*, 2014; and ref. therein). The major problem with that technique is that electron irradiation sensitive material might become amorphous during acquisition of the diffraction pattern due to irradiation damage.

With nanocrystalline and electron irradiation sensitive material there is only one option to get structural data. High-resolution lattice fringe images can be acquired from different low-indexed zone-axis orientations with very short (0.1 s) acquisition time. From the lattice fringe image a diffraction pattern can be calculated using fast Fourier Transform (FFT) which provides the same information as an electron diffraction pattern.

3.1.1. Diffraction contrast in TEM

Without the use of an objective aperture, the contrast of TEM bright-field image is very poor because only mass absorption contrast is relevant for the image contrast. The objective aperture is located at the back focal plane where the diffraction pattern is displayed. There are objective apertures available in the range 10–800 μm in diameter. Placing the objective aperture with the smallest diameter (10 μm) around the central spot representing the non-scattered electrons from the primary beam excludes all other diffracted electrons from image formation (Fig. 12a). That kind of image is called a bright-field (BF) image with strong image contrast. The second option to place an objective aperture is to position it over one of the diffracted intensities (Fig. 12b). This imaging mode is called dark-field (DF) imaging. The diffracted intensity only is used for image formation. For example, dark-field imaging is useful for imaging a particular crystal in fine-grained material, exsolution lamellae, twins, dislocation lines, and grain- or phase boundary planes.

Another option is to place a large objective aperture such that it includes the undiffracted intensity together with different scattered intensity with the objective aperture centred at the undiffracted primary beam. Under these conditions all diffracted intensity within the aperture plus the undiffracted intensity contribute to image formation. That kind of imaging is called phase contrast imaging. It is used for high-resolution imaging. More details about phase contrast imaging will be presented in the section on high-resolution imaging.

Diffraction contrast and the basic physics of this method are described in more detail elsewhere (Hirsch *et al.*, 1977; Edington, 1975a,b; Williams and Carter, 1996; Fultz and Howe, 2001).

3.2. Information derived from electron diffraction patterns

Electron diffraction patterns contain the following important structural information:

Crystalline or non-crystalline state
Single crystal or polycrystal (*e.g.* nano-diamond)
Lattice parameters

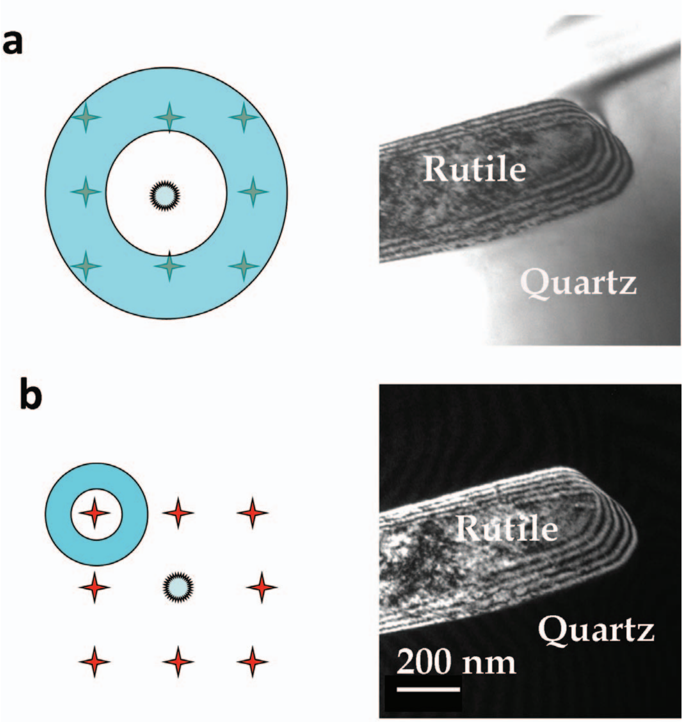

Fig. 12. Bright-field (BF) and dark-field (DF) imaging in TEM. (a) In bright-field imaging the objective aperture excludes all diffracted intensity from image formation. Only the intensity of the primary electron beam passes through the objective aperture. The corresponding BF image of a rutile needle in quartz is shown on the right hand side of the image. The sequence of dark and bright contrasted lines along the interfaces represents thickness fringes. The sequence of contrast lines starts with bright contrast followed by a dark contrast. (b) Using one of the diffracted intensities for image formation only, excluding all other intensities with the objective aperture is called DF imaging. The corresponding DF image on the right hand side of the image shows again the alternating bright and dark contrast at the interface rutile/quartz. In the dark-field image the sequence of thickness contrast starts with dark contrast followed by bright contrast lines.

Crystal symmetry and space group
Ordering of atoms in the crystal lattice (*e.g.* hydrous olivine)
Orientation relationship of two crystals (*e.g.* Mg-ferrite and ferro-periclase)
Exsolution by spinodal decomposition (*e.g.* satellite reflections feldspar)
Mosaic crystals

3.2.1. Crystalline or non-crystalline state

Diffraction patterns display the crystalline or non-crystalline state of the material investigated. Crystals reveal regular and symmetric discreet scattering intensities whereas non-crystalline matter shows only broad and diffuse scattering intensity rings. However, nanocrystalline materials with randomly oriented crystals and average grain size of <5 nm also display only broad scattering intensity along Debye-Scherrer rings. There is substantial peak broadening in X-ray diffraction analysis with decreasing grain size from 100 to 1 nm (Glocker, 1971). However, peak broadening can also be caused by elastic strain in the crystals. If there is only broad scattering intensity in the diffraction pattern the amorphous or nanocrystalline state of the material can be verified with high-resolution lattice fringe imaging searching for the presence or absence of lattice fringes. Only if there are no lattice fringes visible is it possible to identify unambiguously the non-crystalline state of a material (Toy *et al.*, 2015). More detailed information about diffraction line broadening can be found elsewhere (Glocker, 1971; Fultz and Howe, 2001).

3.2.2. Single crystal or polycrystalline material

The diffraction pattern can also indicate the presence of a single crystal or polycrystalline material. Randomly oriented crystals create Debye-Scherrer rings in the electron diffraction pattern. Each radius of the individual rings corresponds to a particular $\vec{g}$ vector in reciprocal space and corresponding d spacing in real space can be calculated from equation 10. Usually, the Debye-Scherrer rings are not completely occupied with diffraction intensity because the number of scattering crystals in a typical TEM foil is too small to produce enough diffraction spots to form a complete ring pattern. Only in the case of nanocrystalline material is there a chance to observe the Debye-Scherrer rings completely occupied. If the individual diffraction spots on the ring cluster it suggests preferred orientation of the individual crystals. This has been demonstrated using the electron diffraction pattern (SAED) from nanocrystalline diamond included in orthopyroxene (Wirth and Rocholl, 2003). There is scattering intensity on rings with different radii. These rings can be assigned to (111), (022) and (113) diamond reflections. The clustered intensity on the individual rings suggests a weak preferred orientation relationship between the individual nanodiamonds.

A special case of oriented nanocrystals in a host mineral is presented in Fig. 13a,b. A ferro-periclase inclusion in diamond hosts oriented nanocrystalline precipitations of Mg-ferrite along ancient dislocation lines (Fig. 13a) (Wirth *et al.*, 2014). The diffraction spots from the ferro-periclase host are bright with much weaker spots in between that represent the nanocystalline Mg-ferrite (Fig. 13b). Nanocrystalline Mg-ferrite behaves like a single crystal. The unit-cell parameter of cubic Mg-ferrite is 0.858 nm and that of the host cubic ferro-periclase is 0.422 nm. Therefore, in reciprocal space the reflections of Mg-ferrite are located half way between the host ferro-periclase reflections. Both phases have the same zone axis orientation [$\bar{1}$01].

3.2.3. Unit-cell parameters

Unit-cell parameters can be derived from electron diffraction patterns acquired in suitable low-indexed zone-axis orientation. In those cases where there are only nanocrystals (<50 nm), which are sensitive to electron irradiation damage, diffraction patterns can be obtained only from high-resolution lattice fringe images in low-indexed zone axis orientation. Fast Fourier Transform processing converts the lattice fringe image into a diffraction pattern. The evaluation of several diffraction patterns from

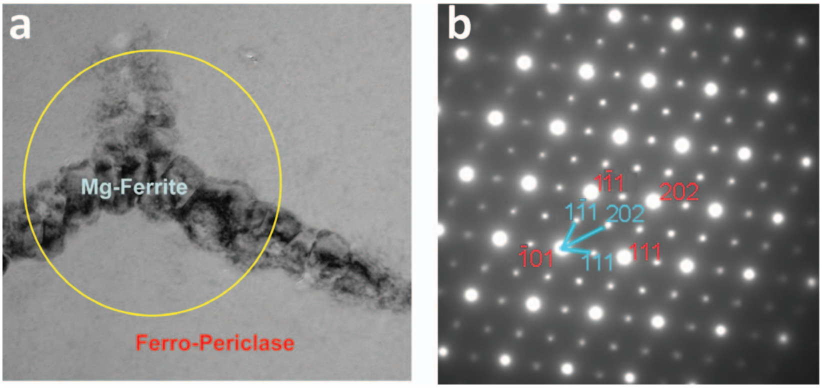

Fig. 13. Nanocrystals of Mg-ferrite precipitated in a ferro-periclase inclusion in deep-seated diamond from Juina, Brazil. (a) BF image of Mg-ferrite with dark diffraction contrast patches in a homogeneous ferro-periclase matrix. Circle indicates the volume used for the electron diffraction pattern. (b) SAED pattern with strong scattering intensity from the ferro-periclase matrix and the weaker scattering intensities from the Mg-ferrite inclusions. Note the rigorous orientation relationship between inclusion and host.

different zone axis orientation can provide the unit-cell parameters of a crystal. This technique has been applied successfully to nanocrystalline inclusions (*e.g.* phase Egg) in diamond and oriented nanocrystalline inclusions of (Mg,Fe,Cr)TiO_3 perovskite in olivine (Wirth and Matsyuk, 2005; Wirth *et al*., 2007). If the nanocrystals are randomly oriented that procedure can be very time consuming as in the case of phase Egg. However, when the nanocrystals are strictly oriented with respect to the host (*e.g.* (Mg,Fe,Cr)TiO_3 perovskite in olivine) then there is a chance to observe the very weak scattering intensity of the nanocrystals in a conventional SAED pattern. In that case the scattering intensities from the individual scattering nanocrystals add up to more intensive and finally visible scattering intensity in the diffraction pattern. Image plates are very useful as the recording medium because of the very high dynamic range of the image plates. That means, it is possible to observe very weak scattering intensity from the nanocrystals beside the very strong scattering intensity from the host.

If the nanocrystals are not electron irradiation sensitive the precession technique described above provides the best results in resolving the crystal structure (*e.g.* Koch-Müller *et al*., 2014; and references therein). The precession technique is also most valuable for the determination of space group and crystal symmetry. Usually, the TEM samples are not thin enough (<<50 nm) to apply the kinematic scattering theory, which calculates the scattering amplitude scattered by a crystal under conditions in which the amplitude of the scattered wave is a small fraction of the incident wave (Hirsch *et al*., 1977). If the conditions of a thin foil and single scattering of the primary electron are not fulfilled, the square of the scattering amplitude (which is the scattering intensity),

$$\text{Amplitude} = \Phi g = \frac{\exp(2\pi ikr)}{r} F(\Theta \tag{11}$$

$$F(\Theta) = \sum_j f_j \times e^{i\pi(hx_j + k_y + lz_j)} \tag{12}$$

does not represent the true scattering intensity. Measuring the real scattering intensity is the basic requirement for structure calculations. In equation 11 $F(\Theta)$ is the scattering amplitude from the unit cell, Φ_g is the scattering amplitude of the crystal with r representing the periodic distance in a lattice and k is the wave vector. The indices (hkl) represent the reflecting lattice planes and (x, y, z) are the coordinates of the individual atoms in the unit cell. The atomic scattering factor for an individual atom j is f_j in equation 12. Electron scattering in the usually thicker TEM foils (100−150 nm) is theoretically treated by the dynamical scattering theory. The dynamical theory considers the interaction of the electron wave with the periodic potential of the atoms in the crystal, which results in an attenuation of the scattered intensity with increasing sample thickness and an interaction of the primary electron wave with the scattered electron wave. A detailed treatment of the kinematic and dynamic theory of electron scattering can be found elsewhere (Edington, 1975a,b; Hirsch *et al.*, 1977; Williams and Carter, 1996).

3.2.4. Crystal symmetry and space group

Because we usually use relatively thick samples (100−150 nm) we have to be aware that due to multiple scattering, the extinction rules, which are defined by the crystal symmetry, cannot be applied. That means that, in electron diffraction patterns, forbidden reflections might occur. Olivine is a good example to demonstrate that. The space group of olivine with an orthorhombic structure is *Pbnm*. That space group does not allow reflections such as (100), (010) and (001). However, in real diffraction patterns they might be present. The fact that forbidden reflections might occur in electron diffraction patterns and in FFT from high-resolution lattice fringe images is important when evaluating diffraction pattern and comparing the observed *d* spacing with the calculated *d* spacing. Therefore, it is necessary to calculate also the forbidden *d* spacing otherwise it is very often impossible to index the observed diffraction pattern correctly and thus identify a phase.

3.2.5. Ordering

Hydrous olivine is an example to demonstrate ordering processes occurring in a crystal causing a change in crystal symmetry. Mg vacancies in olivine charge-compensated by hydrogen (hydrous olivine) occur at random when they form in the Earth′s mantle. Due to the high temperature in the mantle, the Mg vacancies become mobile and start ordering in the crystal structure along the (100) plane, thus forming a hydrous olivine super structure Hy-2a (Khisina and Wirth, 2002). Hydrous olivine was observed as oriented thin lamellae (<50 nm wide) in olivine. In high-resolution lattice fringe images the lattice fringes of hydrous olivine show a completely different pattern from that of olivine (fig. 5a in Khisina and Wirth, 2002; Churakov *et al.*, 2003)). Hydrous olivine is very sensitive to electron irradiation damage and therefore the contrast related to hydrous olivine disappears rapidly. Because there were many of the hydrous olivine lamellae present, and all of them had the same orientation with respect to the olivine host SAED pattern could be acquired successfully. SAED diffraction patterns from such olivine display weak and streaked diffraction intensity additional to the strong spots of the host olivine. The streaks extend normal to the lamellae of hydrous olivine. It is well known in TEM investigations that thin lamellae cause streaking in the electron diffraction normal to the lamellae (Hirsch *et al.*, 1977). The strong olivine reflections in that sample oriented with the [010] zone axis of olivine parallel to the electron beam are the allowed reflections based on the space group *Pbnm* ((200); (002); fig. 7a in Khisina and Wirth, 2002). However, in between there are forbidden reflections of (100) and (001) visible with much less intensity. In between the (001) reflection and the primary beam spot appears an additional spot thus indicating a new reflecting plane with the *d* spacing of $2 \times d_{001}$. Ordering of the Mg vacancies creates a change in crystal symmetry thus producing additional reflections in electron diffraction.

3.2.6. Satellite reflections from spinodal decomposition in alkali-feldspar

If hypersolvus alkali feldspar of intermediate composition is brought into the two-phase equilibrium domain by cooling, it tends to exsolve forming perthite, micro- or cryptoperthite, depending on the characteristic dimensions of the exsolved phases (Abart *et al.*, 2009). Exsolution of a new stable phase from a host mineral may occur by nucleation and growth or by spinodal decomposition (Cahn, 1968). In the final state of the exsolution it is not possible to discriminate from the microstructure whether the exsolution was a spinodal or a nucleation and growth process. However, spinodal decomposition is an uphill diffusion process that in the initial state displays a peculiar microstructure in TEM. The most striking feature of spinodal decomposition microstructure is the presence of very narrow, lens-shaped contrast in bright- and dark-field images (Fig. 14a). The electron diffraction pattern of such a crystal displays a single crystal pattern. However, the reflections show satellites normal to the lens-shaped contrast in the bright-field image indicating the spinodal decomposition lamellae (Fig. 14a). The distance between two satellite spots in reciprocal space of the diffraction pattern can be converted into the mean width of the lamellae in real space using the same procedure of transforming the imaging vector in a diffraction pattern into *d* spacing.

The same information about the mean width of the lamellae can be obtained from intensity profiles across the lamellae in dark-field images (Fig. 14b).

3.2.7. Mosaic crystals

A mosaic crystal is basically a single crystal that is composed of very small (<<100 nm) individual crystalline blocks that are slightly misoriented in relation to each other. In nature, such mosaic crystals commonly form when strongly metamict zircon is hydrothermally treated. The newly formed zircon is composed of individual zircon nanocrystals with almost identical crystallographic orientation. Electron diffraction patterns of mosaic crystals show diffraction intensity that is smeared and distorted (Geisler *et al.*, 2004; Anderson *et al.*, 2008). Mosaic crystals of phase Egg have been reported as inclusions in diamond (Wirth *et al.*, 2007). Figure 15 shows an example of a

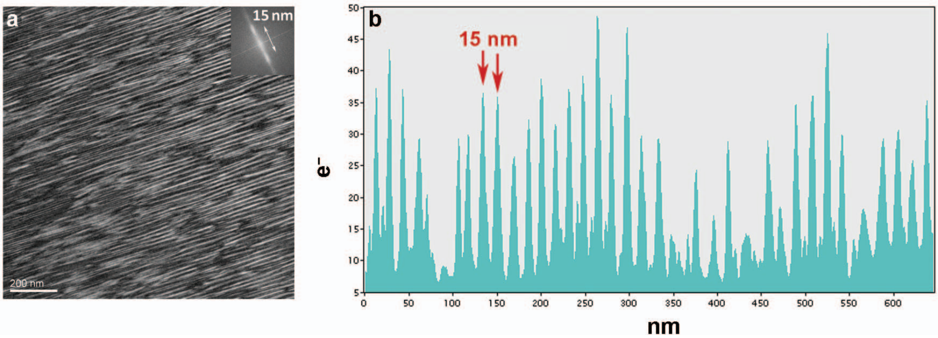

Fig. 14. Spinodal decomposition in alkali feldspar. (a) TEM BF image of spinodal exsolution lamella in alkali feldspar. The inset in the upper right part shows a Fast Fourier Transform (FFT) of the BF image. This is not a high-resolution lattice fringe image. The diffraction spots in the FFT are smeared thus indicating a slightly variable width of the lamellae. The distance between the diffraction spots (maxima from the intensity profile along the FFT) indicates an average lamella thickness of 15 nm. (b) Intensity profile across the image in 14a showing the same average distance between the spinodal decomposition lamellae.

mosaic crystal of phase Egg. In that case several individuals, each <50 nm in size and with almost the same crystallographic orientation are joined thus forming a larger single crystal. Nanometre-sized mosaic crystals are more common in nature. They are usually observed when crystal formation did not occur by nucleation and growth but by assembling precursors to stable crystals. This is referred to as non-classical crystallization (Teng, 2013). Another example of mosaic crystal are nanometre-sized anatase particles forming chains of much larger crystals (Penn and Banfield, 1999). In a recent paper by Schäbitz *et al*. (2015) the formation of nanometre-sized crystals of Calcite III, a high-pressure form of calcite, was also related to the formation of mosaic crystals from nanometre-sized precursor phases.

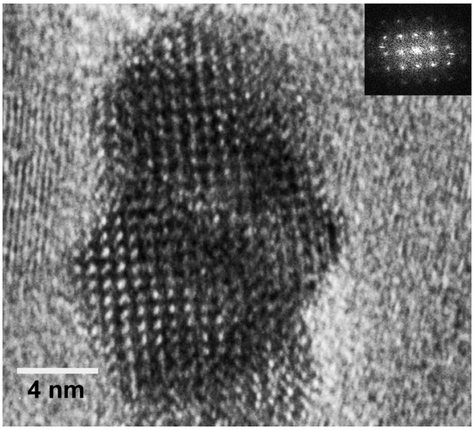

Fig. 15. High-resolution lattice fringe image of nano-inclusions of phase Egg observed as inclusions in diamond from Juina, Brazil. Nanocrystals of phase Egg are attached to each other thus forming a larger mosaic crystal with the individual crystals slightly misoriented. The diffraction patterns inserted (FFT) show that the crystals represent a single crystal.

3.3. High-resolution transmission electron microscopy (HRTEM)

An electron wave passing through a sample interacts with the atoms and electrons of the sample resulting in different scattering events. These interactions induce slight phase shift of the scattered electron waves. Using a high-resolution mode of the TEM, a larger objective aperture allows the primary electron wave plus several scattered electron waves to pass through and recombine. The recombination of the scattered waves that have experienced slight phase shift with the unscattered wave creates intensity differences from point to point in the image. The intensity differences are called phase contrast. Phase contrast effects become important when image details <1.5 nm are resolved, and that applies for high-resolution imaging.

More sophisticated theoretical treatments of phase shifts of the scattered waves caused by the atoms and electrons of the sample are found elsewhere (Cowley and Iijima, 1976). Consider a diffraction pattern from a crystal in which only the primary beam and two strongly excited diffraction spots are visible. If an objective aperture be placed in such a way that it allows only the primary beam and the two diffracted beams to pass through, then, after recombination, a high-resolution image with periodic changes in intensity (fringes) results. The periodicity of the fringes is inversely proportional to the distance between the two diffraction spots in the diffraction pattern thus corresponding to the periodicity d_{hkl} of the lattice planes in the crystal structure (Fig. 16). The position of the maxima and minima (intensity) in the lattice fringe image depends on the phase shift of the two diffracted beams. The phase shift depends on the sample thickness and the crystallographic orientation of the sample. The contrast – dark or bright – depends on sample thickness z and deviation from the Bragg position (deviation parameter, s). It is important to note that the location of the reflecting lattice planes in the crystal does not coincide with the lattice fringes. If the sample thickness z changes, dark fringes might be replaced by bright fringes. The reason for that behaviour is the dependence of the intensity of the primary electron beam and the diffracted beam having passed through the sample from the sample thickness z. That effect is commonly observed in wedge-shaped samples that have been prepared by argon ion milling. Additional image shift is caused by spherical aberration of the objective lens c_s, astigmatism of the objective lens, deviation parameter s and defocus, Δf. High-resolution imaging requires thin foils and perfect alignment of the crystal with a low-indexed zone axis parallel to the optical axis of the TEM. Perfect alignment of the crystal is accomplished when the diffracted intensity in the electron diffraction pattern is almost equal (Fig. 17).

The transfer of information from the sample into the diffraction pattern and into the phase contrast image is described by the contrast transfer function (CTF).

$$H(\mathbf{u}) = A(\mathbf{u}) \times E(\mathbf{u}) \times B(\mathbf{u}) \qquad (13)$$

In equation 13, $\mathbf{u}$ is a reciprocal lattice vector or the spatial frequency ($1/d_{hkl}$) for a particular direction in the crystal structure. High frequencies correspond to short distances in the lattice. In high-resolution imaging we are looking for high spatial frequencies, and therefore, we need to use a large objective aperture to include these

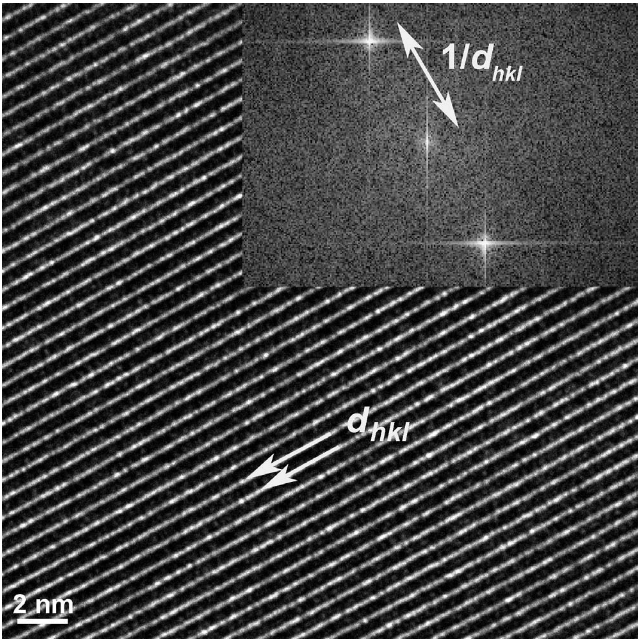

Fig. 16. High-resolution lattice fringe image. The distance between the bright and dark contrasts represents the *d* spacing of the reflecting lattice planes. The corresponding diffraction pattern (FFT) is given in the inset. Note that the distance between the primary electron beam and the diffracted beam is $1/d_{hkl}$ (reciprocal space). The *d* spacing in the image is real space d_{hkl}.

high spatial frequencies in the image formation. $A(\mathbf{u})$ is the aperture function. The objective aperture cuts off the high spatial frequencies greater than the diameter of the aperture. $E(\mathbf{u})$ is the envelope function describing properties of the lens itself. $E(\mathbf{u})$ represents the attenuation of the electron wave (envelope function) caused by

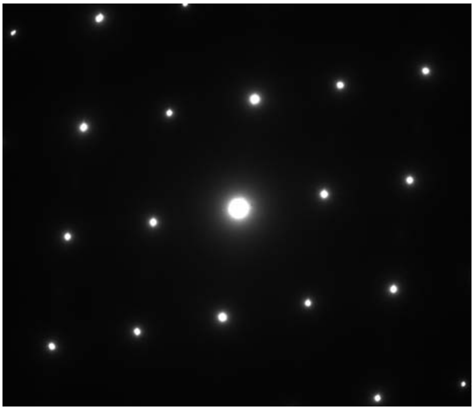

Fig. 17. Electron diffraction pattern with a low-indexed zone axis aligned almost parallel to the electron beam. Note that under that conditions the scattered intensity of the different spots is approximately the same.

instabilities of the electron current (I) and instabilities in the accelerating voltage (V). The most important term in the contrast transfer function $H(\mathbf{u})$ is the term $B(\mathbf{u})$, which considers the aberration of the objective lens. $B(\mathbf{u})$ is expressed as:

$$B(\mathbf{u}) = \exp i\chi(\mathbf{u}) \tag{14}$$

$$\chi(\mathbf{u}) = \pi \times \Delta f \times \lambda \times \mathbf{u}^2 + 1/2\pi \times c_s \times \lambda^3 \times \mathbf{u}^4 \tag{15}$$

In equation 15, Δf is the defocus used, c_s is the spherical aberration coefficient, λ is the wavelength of the electrons and $\mathbf{u}$ is the spatial frequency (reciprocal lattice vector $1/d_{hkl}$). To solve equation 14 the Euler formalism (equation 16) is applied:

$$B(\mathbf{u}) = \cos \chi(\mathbf{u}) + i\sin\chi(\mathbf{u}) \tag{16}$$

The term $\cos \chi(\mathbf{u})$ describes the amplitude contrast and $i\sin \chi(\mathbf{u})$ represents phase contrast.

Figure 18 is the contrast transfer function (CTF) calculated for defocus $\Delta f = -68$ nm, spherical aberration coefficient $c_s = 1.3$ mm and electron wavelength = 0.00251 nm. For $\sin \chi(\mathbf{u}) = 0$ no information will be transferred from the sample to the image. With increasing spatial frequency the graph of $\sin \chi(\mathbf{u})$ gets negative approaching the value -1. Between the spatial frequencies 1.5 (nm^{-1}) and 3.5 (nm^{-1}) that function $\sin \chi(\mathbf{u})$ shows high negative values approaching -1 and thus provides a broad band of good transmittance. That is the range of spatial frequencies where the most information is transferred from the sample to the image and it results in positive phase contrast. At $\mathbf{u}$ = 4.2 (nm^{-1}) the CTF in Fig. 18 is 0, and then changes into positive phase contrast. When the graph of the function $\sin \chi(\mathbf{u})$ crosses the spatial frequency axis $\mathbf{u}$ (nm^{-1}) for the first time the value of the function is 0 and that value of $\mathbf{u}$ (nm^{-1}) defines the point resolution of the TEM. For $\Delta f = -68$ nm, spherical aberration coefficient, $c_s = 1.3$ mm and electron

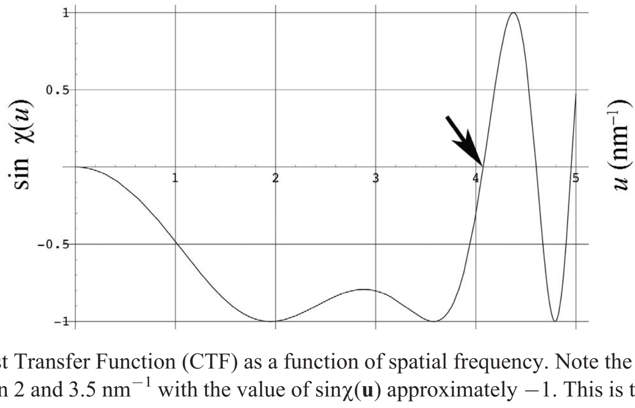

Fig. 18. Contrast Transfer Function (CTF) as a function of spatial frequency. Note the plateau region of the CTF between 2 and 3.5 nm^{-1} with the value of $\sin\chi(\mathbf{u})$ approximately -1. This is the region of CTF where most of the information is transferred from the object to the image. The first transect of the graph of CTF with the spatial frequency axis (arrow) defines the point resolution of the TEM. The CTF presented here is defined for a spherical aberration coefficient $c_s = 1.3$ mm and Scherzer defocus is -68 nm. The point resolution is 0.25 nm.

wavelength = 0.00251 nm; the point resolution is 0.25 nm (*e.g.* FEI TECNAI F20 X-Twin). In a TEM with spherical aberration coefficient c_s = 2 mm (*e.g.* Philips CM 200) the point resolution will decrease to 0.303 nm (Fig. 19). The CTF also changes dramatically with changing defocus Δf. The crucial question is now at which defocus the CTF is maximized? The optimal defocus has come to be known as 'Scherzer' defocus Δf_{Sch}.

$$\Delta f_{\mathrm{Sch}} = -1.2(c_s\lambda)^{1/2} \tag{17}$$

The contrast transfer function $H(\mathbf{u}) = A(\mathbf{u}) \times E(\mathbf{u}) \times B(\mathbf{u})$ is modified if we add the contribution from the envelope function $E(\mathbf{u})$ to the term $B(\mathbf{u})$. $E(\mathbf{u})$ can be considered as a damping function. $E(\mathbf{u})$ considers chromatic aberration, which is caused by instabilities in the high voltage and the objective lens current. In the CTF without envelope function the oscillations of the function sin $\chi(\mathbf{u})$ principally could extend to unlimited values of $\mathbf{u}$ (nm^{-1}). In reality, if the envelope function is applied, the function sin $\chi(\mathbf{u})$ dies off at a certain value of $\mathbf{u}$ (nm^{-1}). Beyond that value there is no more information in the image (Fig. 20). The value of $\mathbf{u}$ (nm^{-1}) where CTF approaches 0 is defined as the information limit of the TEM. Beyond the information limit there is no meaningful interpretation of any feature in the image possible.

There are two important imaging limits represented by the CTF. The first crossover of the graph of the function sin $\chi(\mathbf{u})$ with the $\mathbf{u}$ (nm^{-1}) axis defines the point resolution and the damping of the function sin $\chi(\mathbf{u})$ to almost 0 by the envelope function, which defines the information limit. If the information limit is beyond the Scherzer resolution limit (point resolution), image simulation software is needed to interpret any detail beyond the Scherzer limit (Williams and Carter, 1996).

From high-resolution lattice-fringe images we can easily derive the spatial frequencies $1/d_{hkl}$ by applying a FFT. The FFT is a calculated diffraction pattern from the lattice fringe image. The diffraction spots with a vector length of $1/d_{hkl}$ are calculated from the information stored in the whole image. Therefore, they provide more precise d-spacing determinations than measuring the d spacing directly from

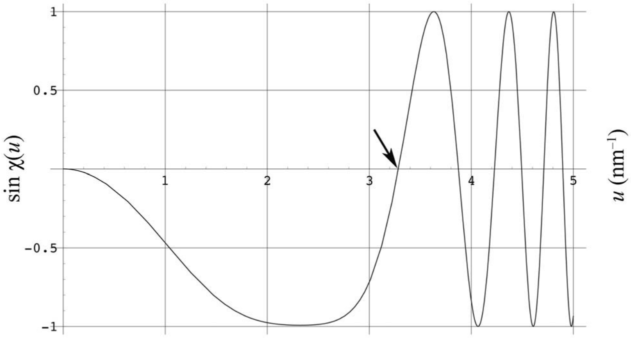

Fig. 19. Dependence of the contrast transfer function CTF on the spherical aberration coefficient c_s (c_s = 2 mm). The CTF at the same Scherzer defocus results in a smaller plateau region and a point resolution of 0.303 nm.

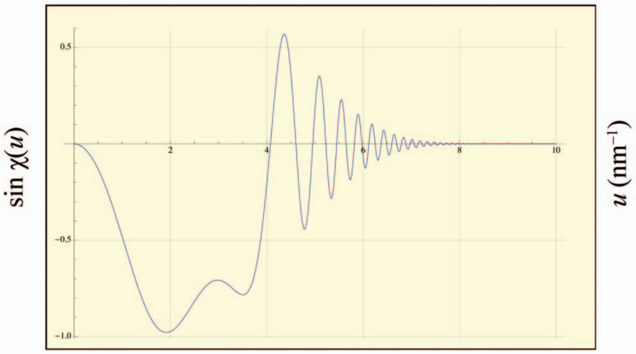

Fig. 20. CTF with the envelope function $E(\mathbf{u})$ applied, which considers chromatic aberration due to instabilities in high-voltage and electron current. Without the envelope function the CTF would oscillate and extend to unlimited values of **u** (nm^{-1}). With the envelope function applied the CTF dies off at a certain value of **u** (nm^{-1}). That value defines the information limit of the TEM.

some locations in the lattice fringe image. The d spacing calculated from the FFT and the angles between the spots (diffraction vectors) in the diffraction pattern can be used to identify a particular phase unambiguously. It is only necessary to compare the observed d_{hkl} and the adjacent angles between the diffraction vectors with calculated d spacings and angles. At that point it needs to be emphasized that only in the case of a very thin sample (<30 nm), where we can apply kinematic theory of electron diffraction (Hirsch *et al*., 1977) do the extinction rules based on the space group of a crystal apply. In thicker samples it is expected that forbidden reflections occur and contribute to the diffraction pattern and to the lattice fringe image. Consequently, a diffraction pattern or FFT can only be indexed and attributed to a particular crystal if we include forbidden reflections.

However, if we want to interpret contrast details in the high-resolution image with respect to individual atom columns or crystal structural details, image simulation is required. Such an image simulation requires the knowledge of the crystal structure, the experimental conditions such as sample thickness z, defocus Δf, deviation parameter s, spherical aberration of the objective lens c_s and the wavelength of the primary electron λ. Only if the simulated image based on the imaging parameters matches the experimental image is a meaningful interpretation of the contrast possible (*e.g.* Marquardt *et al*., 2011; their fig. 2). More detailed information about high-resolution imaging in TEM is provided elsewhere (Buseck *et al*., 1988; Spence, 1988; Carter and Williams, 1996, Fultz and Howe, 2001).

High-resolution lattice-fringe imaging is a powerful tool in geosciences to identify minerals, even nanometre-sized crystals. It is not, however, a tool for crystal structure analysis. Usually, silicate minerals are sensitive to electron irradiation damage and therefore become amorphous very quickly under the electron beam. Quartz, a most common silicate is especially sensitive and transforms into a non-crystalline state very rapidly. To acquire a high-resolution lattice-fringe image from quartz a very short exposure time (<0.5 s) is required; after that the imaged volume is amorphous. With nanometre-sized crystals convergent beam electron diffraction (CBED) would be the right technique to acquire an electron diffraction pattern. However, focusing the electron beam for CBED would immediately render the structure amorphous. CBED is not an option for most silicate nanocrystals. The only technique to get structural information from nanoinclusions in minerals (*e.g.* inclusions in diamond) is high-resolution lattice fringe imaging and subsequent calculation of FFTs. This technique has been applied effectively in numerous cases (Wirth *et al.*, 2005, 2007, 2013; Khisina and Wirth, 2002; Kaminsky *et al.*, 2009; Schäbitz *et al.*, 2015).

4. Microstructural features observed in TEM

4.1. Grain shape

The grain shape of micrometre- or nanometre-sized grains can be displayed very well in bright-field or dark-field images. In the dark-field image in Fig. 21 a diamond crystal included in zircon is displayed. The imaging vector for the dark-field image was the (111) reflection of diamond. The alternating bright and dark contrasted layers along the zircon–diamond interface are thickness fringes. It is evident that in some locations the

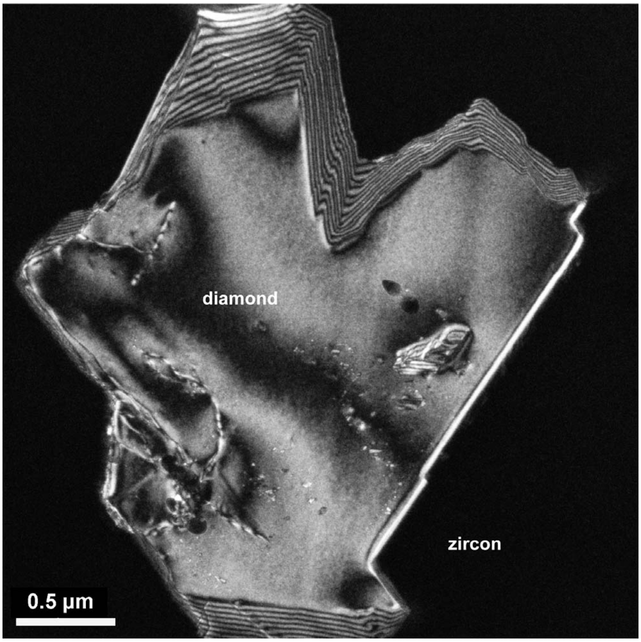

Fig. 21. Dark-field image (DF) of a diamond inclusion in zircon. The interfaces of the diamond crystal are characterized by the alternating dark and bright contrast representing thickness fringes. Note the roughness of the diamond surface and the locally different inclination of the interface that gives the image an almost three-dimensional appearance. A few dislocation lines are also visible in the left part of the diamond.

interface is parallel to the electron beam with no thickness fringes visible whereas in other locations the interface is inclined differently and rather rough. The image appears to be almost three dimensional. The broad dark contrasts on the diamond surface are diffraction contrasts. A few dislocation lines are also visible in the left part of the diamond crystal. The alternating bright and dark contrast of the dislocation in the upper left part of diamond near the interface suggests a steep inclination of the dislocation line with the surface. Zircon is completely dark because the (111) reflection of diamond was used exclusively for the dark-field imaging.

4.2. Twins

Twinning is a common feature in minerals, and TEM is a tool to identify the twin law using electron diffraction and diffraction contrast imaging. In diamond grown by chemical vapour deposition or gas phase condensation {111} nanotwins are very common. These twins are a characteristic microstructural feature of such diamond formation under low-pressure conditions (Shechtman, 1994; Tsuno *et al*., 1994). Recently diamond aggregates found as inclusions in lava from Kamchatka volcanoes have been investigated with TEM. One of the striking microstructural features of these diamonds is intensive twinning along the {111} planes (Fig. 22). Aside from other observations, the presence of nanotwins suggested that these diamonds were formed in local microenvironments in lavas by chemical vapour deposition (Kaminsky *et al*., 2016).

4.3. Symplectites

Symplectites comprise a vermicular intergrowth of usually submicrometre-sized crystals that replace a host mineral at a sharp reaction front. Garnet is a typical example for symplectite formation with anorthite + orthopyroxene and spinel replacing garnet (Degi *et al*., 2010). Another example is majoritic garnet from the Snap Lake kimberlite

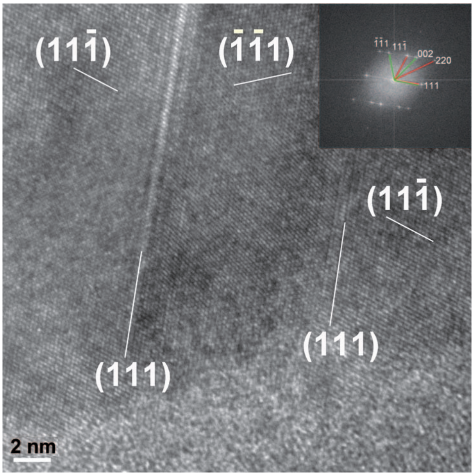

Fig. 22. High-resolution lattice fringe image of nanometre-sized twins in diamond. The twinning plane is the (111) plane in diamond. The twinning is also visible in the diffraction pattern (FFT).

(North West Territories, Canada) that was partially transformed into orthopyroxene + clinopyroxene + Cr-spinel + coesite. The majoritic garnet is separated from the lamellar intergrowths of very narrow lamellae (<50 nm) of Opx + Cpx + Cr-spinel + coesite by a sharp reaction boundary (Fig. 23). Such small lamellae can be identified only using high-resolution lattice fringe imaging combined with EDX analyses. The FFTs from the lattice-fringe images provide structural data (*d* spacing) that can be combined with the chemical composition thus identifying the phases. For example, high-resolution element mapping of the X-ray intensities revealed the presence of a SiO_2 phase, which subsequently was identified from lattice-fringe images as coesite. That majoritic garnet occurs as an inclusion in diamond. During uplift of the diamond to the Earth′s surface pressure and temperature decreased so that majorite became unstable and the transformation started *via* a moving reaction front. Equilibrium of majoritic garnet was achieved during mantle residence time at 1380ºC at 11 GPa (Sobolev *et al.*, 2008).

4.4. Dislocations

Dislocations are crystal defects that can be incorporated in the crystal during crystal growth or during later plastic deformation. The dislocation line and the Burgers vector define a dislocation. There are three different types of dislocations: There are edge dislocations with the Burgers vector normal to the dislocation line; in case of a screw dislocation the Burgers vector is parallel to the dislocation line; and finally, there are dislocation loops with a screw component (Burgers vector parallel to the dislocation line) and an edge component (Burgers vector normal to the dislocation line). Screw dislocations and edge dislocations are basic elements of plastic deformation of materials. Dislocation loops are created by vacancy condensation or by condensation of atoms or molecules on particular lattice planes. More details about dislocations can be found elsewhere (Hull and Bacon, 1984). Dislocations can move along a crystallographic direction in a crystal by a glide mechanism. Usually, plastic deformation

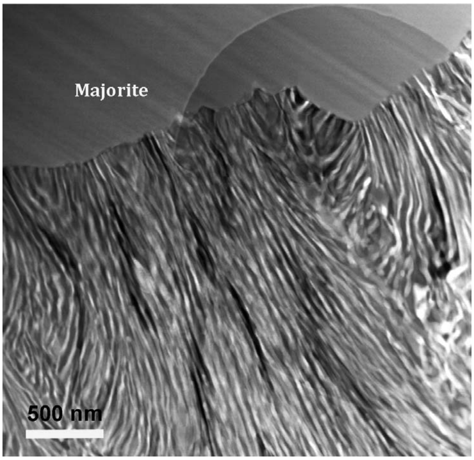

Fig. 23. HAADF image of a symplectite composed of Opx, Cpx, Cr-spinel and coesite replacing a majoritic garnet inclusion in diamond from Slave Craton. The round feature in the background is due to the perforated carbon film on which the TEM lamella rests.

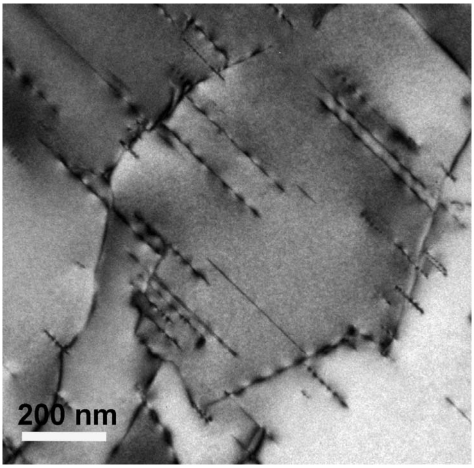

Fig. 24. TEM bright-field image of diamond with dislocation lines. Note that most of the dislocation lines are straight thus indicating deformation of the diamond by dislocation glide.

occurs by dislocation glide. The presence of straight dislocation line contrast in BF- or DF-imaging indicates dislocation glide in TEM (Fig. 24). Very often, in plastically deformed materials parallel dislocation lines are visible simultaneously. The dislocation line visualizes the end of the inserted half-plane in the crystal structure. If atoms are added to the end of the half plane or removed from the half plane the dislocation line contrast starts curving finally resulting in a strongly curved dislocation line. That process is called dislocation climb (Fig. 25). Adding atoms to the half plane or removing atoms from the half plane is a diffusion process that is always thermally activated. A certain threshold energy (*i.e.* the activation energy) that is characteristic of a particular mineral must be overstepped to start the process. That means, if we observe

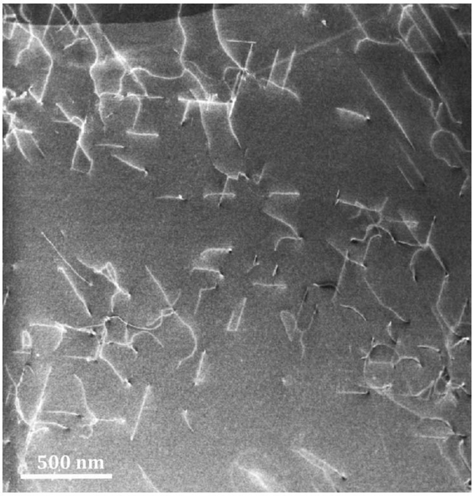

Fig. 25. HAADF diffraction contrast image of diamond. The bright contrasted lines are dislocation lines that are mostly curved and twisted. Such curved dislocations indicate dislocation climb, a thermally activated process suggesting a longer residence time under high temperature after deformation.

predominantly straight dislocation lines (*e.g.* in diamond in Fig. 24) we might conclude that the crystal has been deformed plastically. In the case of diamond that deformation occurred under high-temperature conditions most likely in the upper mantle. However, if only straight dislocation lines are visible we can conclude that the residence time of the diamond under high-temperature conditions was not long. If the diamond had been deformed and had resided for a longer period under high-temperature conditions, the dislocations would have started to climb thus forming strongly curved dislocation lines. In such a particular case we can assume that the diamond has been transported rapidly to the surface after deformation. If the threshold temperature for thermally activated processes such as dislocation climb by diffusion of atoms is known – in the case of quartz it is ~300ºC (Voll, 1976) – we can deduce a temperature estimate for that particular mineral. If the dislocations start moving by glide and climb they can rearrange in the crystal finally reducing the stored energy of the crystal. The dislocations rearrange thus forming walls or cells (Fig. 26). The volume that is defined by the cell wall is free of dislocations. It is a process that is called recovery. The formation of dislocation walls is an early stage of recovery. Continuous movement of dislocations ends up in an arrangement of the dislocations in low-angle grain boundaries, which is shown in Fig. 27.

The misorientation between two grains determines the number of dislocations in a low-angle grain boundary (Heinemann *et al.*, 2005). The transition between small-angle and large-angle grain boundaries was defined by the invisibility of individual dislocation lines. If the number of dislocation lines along a low-angle grain boundary increases repeatedly, at a certain number the dislocation cores will overlap and individual dislocation lines are no longer visible (Gleiter and Chalmers, 1972). Heinemann *et al.* (2005) demonstrated that in olivine there are individual dislocation lines visible even at 21º misorientation. That contradicts the observations in metals and alloys where the transition between low-angle and high-angle grain boundaries is in the range of 10–15º misorientation. The

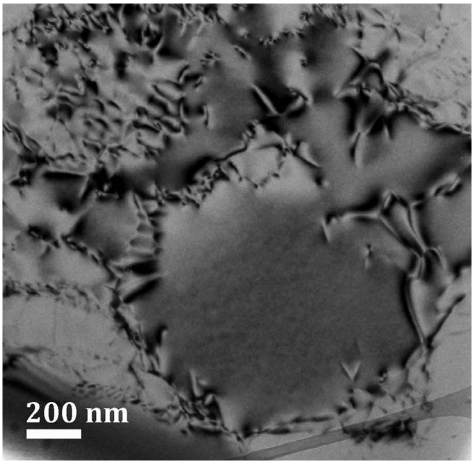

Fig. 26. TEM bright-field image of a calcite crystal with dislocations forming a dislocation-free cell.

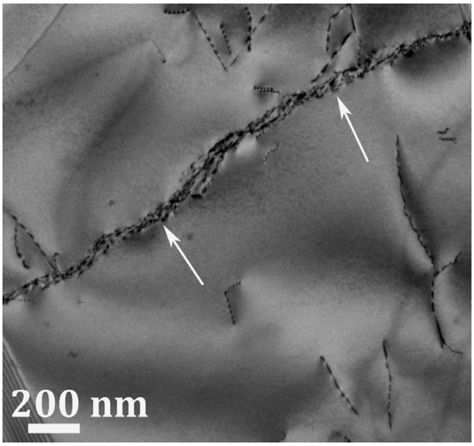

Fig. 27. TEM bright-field image of olivine with dislocations and an array of dislocations (arrows) forming a low-angle grain boundary in olivine. Note the thickness fringes along the surface of olivine.

conclusion from that observation is that the structure of grain boundaries in silicates is different from the structure of grain boundaries in metals. This is quite reasonable because in metals there is no need for charge compensation and in silicates there are rigid units in the form of the SiO_4 tetrahedra.

References

Abart, R., Petrishcheva, E., Wirth, R. and Rhede, D. (2009) Exsolution by spinodal decomposition II: Perthite formation during slow cooling of anatexites from Ngoronghoro, Tanzania. *American Journal of Science*, **309**, 450–475.

Anderson, A.J., Wirth, R. and Thomas, R. (2008) The alteration of metamict zircon and its role in the remobilization of High-Field-Strength elements in the Georgeville granite, Nova Scotia. *The Canadian Mineralogist*, **46**, 1–18.

Aken van, P.A., Liebscher, B. and Styrsa, V.J. (1998) Quantitative determination of iron oxidation states in minerals using Fe $L_{2,3}$-edge electron energy-loss near-edge structure spectroscopy. *Physics and Chemistry of Minerals*, **25**, 323–327.

Brownlee, K.O. (1960) *Statistical Theory and Methodology in Science Engineering*. Wiley, Table II, p 548.

Buerger, M.J. (1970) *Contemporary Crystallography*. Mc-Graw-Hill Book Company, New York.

Buseck, P.R., Cowley, J.M. and Eyring, L. (1988) *High-resolution Transmission Electron Microscopy and Associated Techniques*. Oxford University Press, New York.

Cahn, J.W. (1968) Spinodal decomposition. *Transactions of the Metallurgical Society of AIME*, **242**, 166–180.

Cliff, G. and Lorimer, G.W. (1975) The quantitative analysis of thin specimens. *Journal of Microscopy*, **103**, 203–207.

Churakov, S.V., Khisina, N.R., Urusov, V.S. and Wirth, R. (2003) First principle study of $(MgH_2SiO_4).n(Mg_2SiO_4)$ hydrous olivine structures. I. Crystal structure modeling of hydrous olivine Hy-2a$(MgH_2SiO_4).3(Mg_2SiO_4)$. *Physics and Chemistry of Minerals*, **30**, 1–11.

Cowley, J.M. and Iijima, S. (1976) The direct imaging of crystal structures. Chapter 2.5, pp. 123–136 in: *Electron Microscopy in Mineralogy* (H. Wenk, editor). Springer. Berlin, Heidelberg, New York.

Dégi, J., Abart, R., Török, K., Bali, E., Wirth, R. and Rhede, D. (2010) Symplectite formation during decompression induced garnet breakdown in lower crustal mafic granulite xenoliths: mechanisms and rates. *Contributions to Mineralogy and Petrology*, **159**, 293–314.

Edington, J.W. (1975a) *Electron Diffraction in the Electron Microscope*. Philips Technical Library. Monographs in Practical Electron Microscopy in Materials Science, vol. **2**.

Edington, J.W. (1975b) *Interpretation of Transmission Electron Micrographs*. Philips Technical Library.

Monographs in Practical Electron Microscopy in Materials Science, vol. **3**.

Egerton, R.F. (1996) *Electron Energy-loss Spectroscopy in the Electron Microscope*. Plenum Press, New York.

Fultz, B. and Howe, J.M. (2001) *Transmission Electron Microscopy and Diffractometry of Materials*. Springer, Berlin, Heidelberg, New York.

Garvie, L.A.J., Craven, A.J. and Brydson, R. (1994) Use of electron energy-loss near-edge fine structure in the study of minerals. *American Mineralogist*, **79**, 411−425.

Geisler, T., Seydoux-Guillaume, A-M., Wiedenbeck, M., Wirth, R., Berndt, J., Ming Thang, Mihailova, B., Putnis, A., Salje, E. and Schlüter, J. (2004) Periodic precipitation pattern formation in hydrothermally treated metamict zircon. *American Mineralogist*, **89**, 1341−1347.

Gleiter, H. and Chalmers, B. (1972) *High-angle Grain Boundaries*. Pergamon Press, Oxford, UK.

Glocker, R. (1971) *Materialprüfung mit Röngenstrahlung*. Springer. Berlin Heidelberg New York.

Goldstein, J.I. and Williams, D.B. (1989) Quantitative X-ray analysis. Pp. 155−217 in: *Principles of Analytical Electron Microscopy* (D.C. Joy, A.D. Romig and J.I. Goldstein, editors). Plenum. New York and London.

Heinemann, S., Wirth, R., Gottschalk, M. and Dresen, G. (2005) Synthetic [100] tilt grain boundaries in forsterite: 9.9 to 21.5º. *Physics and Chemistry of Minerals*, **32**, 229−240.

Hirsch, P., Howie, A., Nicholson, R., Pashley, D.W. and Whelan, M.J. (1977) *Electron Microscopy of Thin Crystals*. Reprint of the 1967 issue of the edition published by Butterworths, London. Robert E. Krieger Publishing Co., Inc.

Hull, D. and Bacon, D.J. (1984) *Introduction to Dislocations*. International Series on Materials Science and Technology, Pergamon Press, Oxford, UK.

Joy, D.C., Romig, A.D. and Goldstein, J.I. (1986) *Principles of Analytical Electron Microscopy*. Plenum, New York and London.

Kaminsky, F.V. and Wirth, R. (2011) Iron carbide inclusions in lower-mantle diamond from Juina, Brazil. *The Canadian Mineralogist*, **49**, 555−572.

Kaminsky, F., Wirth, R., Matsyuk, S., Schreiber, A. and Thomas, R. (2009) Nyerereite and nahcolite inclusions in diamond: evidence for lower-mantle carbonatitic magmas. *Mineralogical Magazine*, **73**, 797−816.

Kaminsky, F.V., Wirth, R. and Schreiber, A. (2015) A microinclusion of Lower-Mantle rock and other minerals and nitrogen Lower-Mantle inclusions in a diamond. *The Canadian Mineralogist*, **53**, 83−104.

Kaminsky, F.V., Wirth, R., Anikin, L.P., Morales, L. and Schreiber, A. (2016) Carbonado-like diamond from the Avacha active volcano in Kamchatka, Russia. *Lithos*, doi.org/10.1016/j.lithos.2016.02.021

Khisina, N.R. and Wirth, R. (2002) Hydrous olivine $(Mg_{1-y}Fe_y^{2+})_{2-x}v_xSiO_4H_{2x}$ – a new DHMS phase of variable composition observed as nanometer sized precipitations in mantle olivine. *Physics and Chemistry of Minerals*, **29**, 98−111.

Klein-BenDavid, O., Wirth, R. and Navon, O. (2006) TEM imaging and analysis of microinclusions in diamonds: A close look at diamond-growing fluids. *American Mineralogist*, **91**, 353−365.

Koch-Müller, M., Mugnaioli, E., Rhede, D., Speziale, S., Kolb, U. and Wirth, R. (2014) Synthesis of quenchable high-pressure form of magnetite (h-Fe_3O_4) with composition $^{Fe1}(Fe^{2+}_{0.75}Mg_{0.26})^{Fe2}(Fe^{3+}_{0.70}Cr_{0.15}Al_{0.11}Si_{0.04})_2O_4$. *American Mineralogist*, **99**, 2405−2415.

Kurata, H., Lefevre, E., Colliex, C. and Brydson, R. (1993) Electron energy-loss near-edge structures in the oxygen-edge spectra of transition-metal oxides. *Physical Review B*, **47**, 13763−13768.

Kusiak, M.A., Dunkley, D.J., Wirth, R., Whitehouse, M.J., Wilde, S.A. and Marquardt, K. (2015) Metallic lead nanospheres discovered in ancient zircons. *Proceedings of the National Academy of Sciences of the United States of America (PNAS)*, **112**, 4958−4963.

Logvinova, A.M., Wirth, R., Fedorova, E.N. and Sobolev, N.V. (2008) Nanometre-sized mineral and fluid inclusions in cloudy Siberian diamonds: new insights on diamond formation. *European Journal of Mineralogy*, **20**, 317−331.

Marquardt [Hartmann], K., Ramasse, Q.M., Kisielowski, C. and Wirth, R. (2011) Diffusion in yttrium aluminium garnet at the nanometer-scale: Insight into the effective grain boundary width. *American Mineralogist*, **96**, 1521−1529.

Penn, L.R. and Banfield, J.F. (1999) Morphology development and crystal growth in nanocrystalline aggregates under hydrothermal conditions: insights from titania. *Geochimica et Cosmochimica Acta*, **63**, 1549−1557.

Putnis, A. (1992) *Introduction to Mineral Mciences*. Cambridge University Press, Cambridge, UK.

Rask, J.H., Miner, B.A. and Buseck, P.R. (1987) Determination of manganese oxidation states in solids by electron energy-loss spectroscopy. *Ultramicroscopy*, **21**, 321−326.

Schäbitz, M., Wirth, R., Janssen, C. and Dresen, G. (2015) First evidence of $CaCO_3$-III and $CaCO_3$-IIIb high-pressure polymorphs of calcite: Authigenically formed in near surface sediments. *American Mineralogist*, **100**, 1230−1235.

Shechtman, D. (1994) Twin-determined growth of diamond films. *Materials Science and Engineering*, **A184**, 113−118.

Sobolev, N., Wirth, R., Logvinova, A. and Pokhilenko, N. (2008) An unusual partial retrograde phase transition of majoritic garnet from Snap Lake diamond. In: *Jahrestagung der Deutschen Mineralogischen Gesellschaft* (Berlin 2008), Abstracts.

Spence, J.C.H. (1988) *Experimental High-Resolution Electron Microscopy*. Oxford University Press, Oxford, UK.

Taftø, J. and Zhu, J. (1982) Electron energy-loss near-edge structure (ELNES), a potential technique in the studies of local atomic arrangements. *Ultramicroscopy*, **9**, 349−354.

Teng, H.H. (2013) How ions and molecules organize to form crystals. *Elements*, **9**, 189−194.

Toy, V.G., Mitchell, T.M., Driuventak, A. and Wirth, R. (2015) Crystallographic preferred orientations may develop in nanocrystalline materials on fault planes due to surface energy interactions. *Geochemistry Geophysics Geosystems*, **16**, 2549−2563.

Tsuno, T., Imai, T. and Fujimori, N. (1994) Twinning structure and growth hillock on diamond (001) epitaxial film. *Journal of Applied Physics* , **33**, 4039−4043.

Vincent, R. and Midgley, P. (1994) Double conical beam-rocking system for measurement of integrated electron diffraction intensities. *Ultramicroscopy*, **53**, 271−282.

Voll, G. (1976) Recrystallization of quartz, biotite and feldspars from Erstfeld to the Leventina Nappe, Swiss Alps, and its geological significance. *Schweizer Mineralogisch Petrographische Mitteilungen*, **56**, 641−647.

Williams, D.B. and Carter, C.B. (1996) *Transmission Electron Microscopy*. Plenum Press, New York.

Wirth, R. (2004) A novel technology for advanced application of micro- and nanoanalysis in geosciences and applied mineralogy. *European Journal of Mineralogy*, **16**, 863−876.

Wirth, R. (2009) Focused Ion Beam (FIB) combined with SEM and TEM: Advanced analytical tools for studies of chemical composition, microstructure and crystal structure in geomaterials on a nanometre scale. *Chemical Geology*, **261**, 217−229.

Wirth, R. and Rocholl, A. (2003) Nanocrystalline diamond from the Earth's mantle underneath Hawaii. *Earth and Planetary Science Letters*, **211**, 357−369.

Wirth, R. and Matsyuk, S. (2005) Nanocrystalline (Mg,Fe,Cr)TiO_3 perovskite inclusions in olivine from a mantle xenolith, kimberlite pipe Udachnaya, Siberia. *Earth and Planetary Science Letters*, **233**, 325−336.

Wirth, R., Vollmer, C., Brenker, F., Matsyuk, S. and Kaminsky, F. (2007) Inclusions of nanocrystalline hydrous aluminium silicate "Phase Egg" in superdeep diamonds from Juina (Mato Grosso State, Brazil). *Earth and Planetary Science Letters*, **259**, 384−399.

Wirth, R., Reid, D. and Schreiber, A. (2013) Nanometer-sized Platinum-Group Minerals (PGM) in base metal sulfides: new evidence for an orthomagmatic origin of the Merensky Reef PGE ore deposit, Bushveld Complex, South Africa. *The Canadian Mineralogist*, **51**, 143−155.

Wirth, R., Dobrzhinetskaya, L., Harte, B., Schreiber, A. and Green, H.W. (2014) High-Fe (Mg, Fe)O inclusion in diamond apparently from the lowermost mantle. *Earth and Planetary Science Letters*, **404**, 365−375.